

Supporting Information

Oxygen vacancy dual regulation strategy realizes wide humidity range monitoring of UIO-66(Ce)-derived CeO₂ for intelligent food manufacturing

Huimin Zhang¹, Yu Liu¹, Qi Li¹, Xinlu Zhao¹, Mingze Sun¹, Jiaxin Hou¹, Chuanyu Guo^{1,}, Chaobo Huang³, Xiaoli Cheng¹, Lihua Huo¹, Minghui Yang^{2,*}, and Yingming Xu^{1,*}*

¹ Key Laboratory of Functional Inorganic Material Chemistry, Ministry of Education, School of Chemistry and Materials Science Heilongjiang University, Harbin, 150080, P.R. China. ² School of Environmental Science and Technology, Dalian University of Technology, Dalian, 116024, P. R. China. ³ College of Chemical Engineering, Nanjing Forestry University, Nanjing, 210037, P. R. China.

Corresponding author: Chuanyu Guo: gcy_960831@163.com; Minghui Yang: myang@dlut.edu.cn; Yingming Xu: xuyingming@hlju.edu.cn.

Contents

EXPERIMENTAL SECTION	1
Characterization	1
Manufacturing and testing of humidity sensors	1
Calculations method	2
Figure S1. XPS Ce 3d high-resolution spectra of U6C-0, U6C-10, U6C-20, U6C-30 and U6C-40.	3
Figure S2. TG curve of precursors of U6C-20 in air.	4
Figure S3. SEM (inset are TEM) images of (a) U6C-20-300, (b) U6C-20-500, and (c) U6C-20-600.	5
Figure S4. Nitrogen adsorption-desorption isotherms and pore size distribution of (a) U6C-20-300, (b) U6C-20-400, (c) U6C-20-500, and (d) U6C-20-600.	6
Figure S5. The EPR spectra of U6C-0, U6C-10, U6C-20, U6C-30, and U6C-40 products are prepared by annealing at 400 °C.	7
Figure S8. The contact angle of (a) U6C-20-300, (b) U6C-20-400, (c) U6C-20-500 and (d) U6C-20-600.....	10
Figure S9. Frequency characteristic curve of U6C-20-400.....	11
Figure S10. Continuous response recovery curves of U6C-20-400 in the humidity range of 6% RH to 97% RH at (a) week 1, (b) week 2, (c) week 3, and (d) week 4.	12
Figure S11. Multiple response recovery curves of U6C-20-400 sensors in the 3-6 % RH range.....	13
Figure S12. At 25 °C and 250 Hz, the selectivity testing of the U6C-20-400 sensor for 100 ppm (a) sulfur dioxide, (b) nitrogen, (c) carbon dioxide, (d) ethanol, (e) ammonia, and 10 ppm (f) nitrogen dioxide.	14
Figure S13. (a) Complex impedance spectra of U6C-20-400 at different humidity conditions; (b) Complex impedance spectra of U6C-20-600 at different humidity conditions; (c) Equivalent circuit diagrams for low humidity conditions, medium humidity conditions, and high humidity conditions.	15
Figure S14. (a) Stability test of the U6C-20-400 humidity sensor at 120 °C, 150 °C, 180 °C, and 200 °C for 60 minutes; (b) Long-term stability test of the U6C-20-400 humidity sensor at various temperatures; (c) Impedance change of the U6C-20-400 humidity sensor at various baking temperatures (without food, with a baking time of 5 minutes at each temperature) and at 200 °C for bread slices.	16
Figure S15. A repeatability test of U6C-20-400 was performed to monitor humidity changes caused by baking bread slices at different temperatures.....	17
Figure S16. A repeatability test of U6C-20-400 was performed to monitor humidity changes caused by baking bread slices at the same temperature (180 °C).....	18
Table S1. Analysis of XPS surface species with different acetic acid additions.	19
Table S2. Oxygen vacancy content of U6C-20-300, U6C-20-400, U6C-20-500, and U6C-20-600 ($I_D/I_{F_{2g}}$).	20
Table S3. The element composition and state of U6C-20-300, U6C-20-400, U6C-20-500, and U6C-20-600 as determined by XPS.	21
Table S4. Performance comparison of octahedral CeO ₂ humidity sensor with other humidity sensors.....	22

EXPERIMENTAL SECTION

Characterization.

Thermogravimetric analysis of precursors was performed in air using the Pyris Diamond Thermogravimetric/Differential Thermal Analysis Module (TG-DTA, Pyris-Diamond, Perkin-Elme, USA). The crystal structure of the samples was determined using an X-ray diffractometer (XRD, D8Advance, Bruker, Germany) equipped with Cu K α 1 radiation ($\lambda = 0.15406$ nm). Fourier transform infrared spectroscopy (FT-IR) adopts Nicolet iS10 type manufactured by Thermo in the United States. The morphology and crystalline structure of the samples were examined using a scanning electron microscope (SEM, S-4800, Hitachi, Japan) operated at an acceleration voltage of 5 kV, transmission electron microscopy (TEM, Jem-2010, Jeol) with an acceleration of 200 kV, and high-resolution transmission electron microscopy (HRTEM) and selective area electron diffraction (SAED) techniques. The electron paramagnetic resonance (EPR) spectrum was obtained at T=100 K using a Bruker EMX-plus model spectrometer operating at the X-band frequency. The fluorescence spectrometer (Edinburgh, FLS 980, USA) was used to characterize the PL spectra, and excitation wavelength is 350 nm. X-ray photoelectron spectroscopy (XPS, AXIS ULTRA DLD) measurements were conducted to analyze the elements' surface elemental composition and chemical valence states. The XPS spectra were calibrated using the C 1 s peak at 284.6 eV with the Al K α (energy 1486.4 eV) X-ray source. The hydrophilicity of the materials was tested using a JC20001 contact angle meter. The samples' specific surface area and pore size distribution were determined using the N₂ adsorption test system at 77 K (BET, Tristar 3020, Micromeritics, USA).

Manufacturing and testing of humidity sensors.

The CeO₂ sample was dispersed in ethanol and ground into a paste to prepare the moisture-sensitive element. They were then uniformly coated on the Au fork finger electrodes at a spacing of 50 μ m and dried in a constant temperature oven at 70 °C for one hour. The saturated salt solutions of CsF, LiBr, LiCl, CH₃COOK, MgCl₂, K₂CO₃, Mg(NO₃)₂, KI, NaCl, KCl, and Pb(NO₃)₂ were encapsulated in glass containers and left to stand for at least 48 h to obtain 3%, 6%, 11%, 22%, 32%, 43%, 54%, 68%, 75%, 84% and 97% relative humidity (RH) of the gaseous environment. The preparation and assay process was carried out at 25 °C \pm 2 °C. The CeO₂ sensing elements were exposed to glass containers in different humidity environments, and the moisture sensitivity performance was tested using an LCR digital bridge instrument analyzer (TH 2838 A, Changzhou, China). The whole process is carried out at 25 °C \pm 2 °C. The operating voltage of the moisture-sensitive element is 1 V, and the operating frequency range is 25 Hz - 250 kHz. The impedance value at the initial humidity is Z_a, the impedance value at the measured

humidity is Z_g , and the response is $R=Z_a/Z_g$. The response/recovery time (t_{res}/t_{rec}) is required for a 90% change in the corresponding impedance value. Wet hysteresis coefficient $H_e=\pm\Delta H/2F_{FS}$. ΔH denotes the maximum impedance difference between the adsorption and desorption of water molecules. F_{FS} is expressed as the difference in impedance when the relative humidity changes from 3% to 97 %. In addition, a static gas distribution method was used to test for common interfering gases at 100 ppm. First, the 10 L glass vessel was evacuated. Subsequently, the vacuum glass vessel was filled with an amount of organic solvent (or gas) and allowed to evaporate completely. Finally, fresh air is introduced to equalize the pressure inside and outside the vessel. This method was used to configure 100 ppm of carbon dioxide, nitrogen dioxide, sulfur dioxide, ammonia, nitrogen, and ethanol.

Calculations method^d

Vienna Ab initio simulation package (VASP) was performed for the whole density functional theory calculations. Perdew-Burke-Ernzerhof (PBE) exchange correlation functional was conducted in the projector augmented wave (PAW) method to describe the electron valence and core interactions of atoms. The 10^5 eV of conventional energy and 0.03 eV/Å of force were used for relaxation and self-consistent field (SCF) calculation. A 20 Å vacuum space was constructed to prevent interactions. K-points were set in the model with $(2\times 2\times 1)$ using the Monkhorst-Pack method. The Gibbs free energy of oxygen vacancy defects in CeO_2 were calculated at 298.15 K. The related formula was calculated by $\Delta G=\Delta E + \Delta E_{ZPE} - T\Delta S$, where ΔE , ΔE_{ZPE} and ΔS represent electronic energy, zero-point energy and entropy difference between reactants and products. The zero-point-energies were calculated by frequency analysis. All the entropies of molecules were obtained from the National Institute of Standards and Technology (NIST) database.

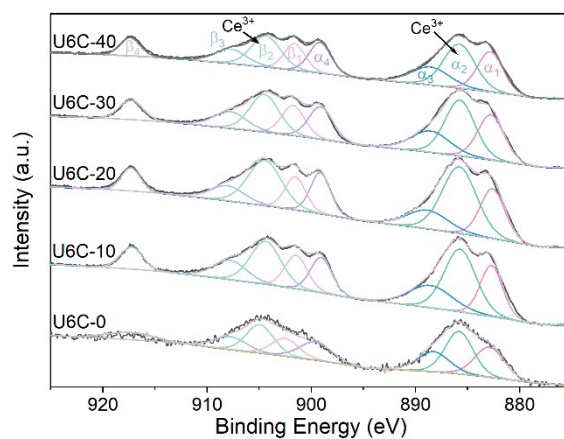


Figure S1. XPS Ce 3d high-resolution spectra of U6C-0, U6C-10, U6C-20, U6C-30 and U6C-40.

Among them, the binding energies of 882.615 eV, 888.161 eV, 899.111 eV, 901.623 eV, 907.423 eV, and 917.313 eV corresponded to the oxidation state of Ce^{4+} . 885.737 eV and 904.423 eV had binding energies corresponding to the oxidation state of Ce^{3+} .

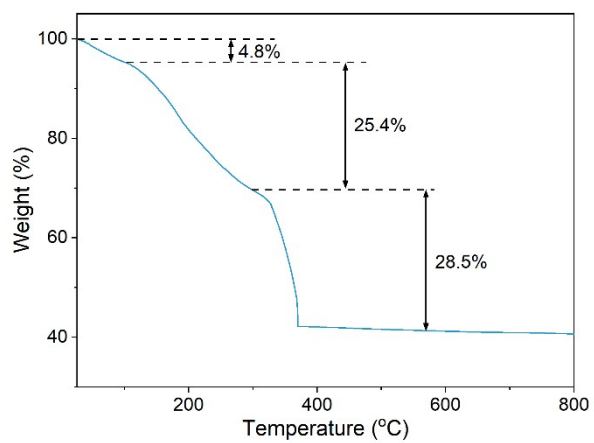


Figure S2. TG curve of precursors of U6C-20 in air.

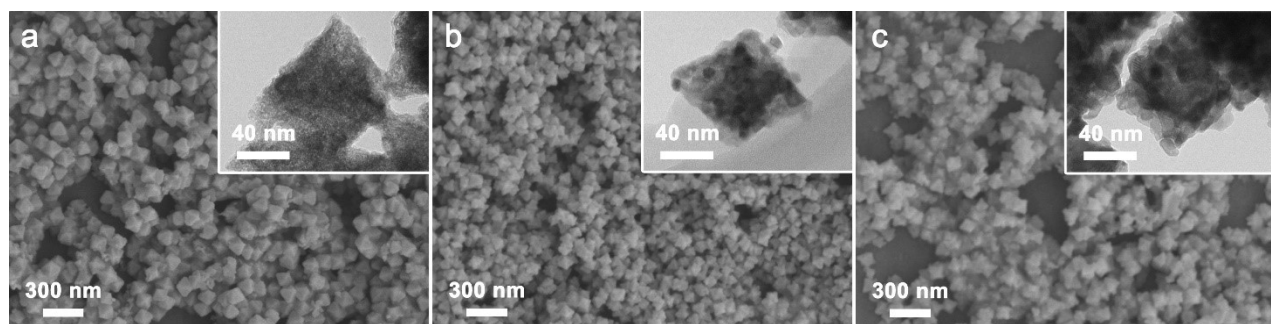


Figure S3. SEM (inset are TEM) images of (a) U6C-20-300, (b) U6C-20-500, and (c) U6C-20-600.

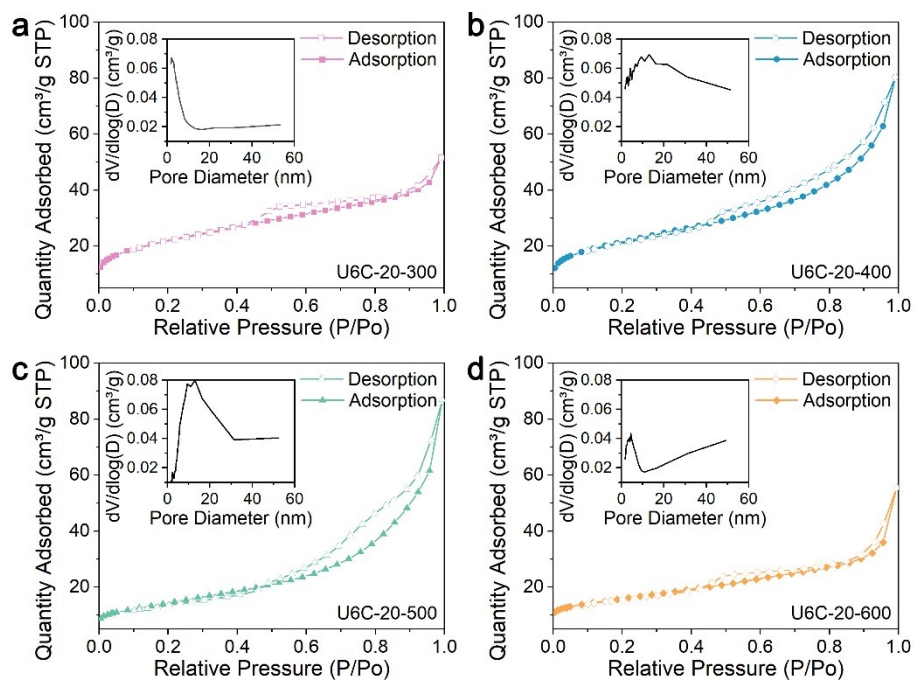


Figure S4. Nitrogen adsorption-desorption isotherms and pore size distribution of (a) U6C-20-300, (b) U6C-20-400, (c) U6C-20-500, and (d) U6C-20-600.

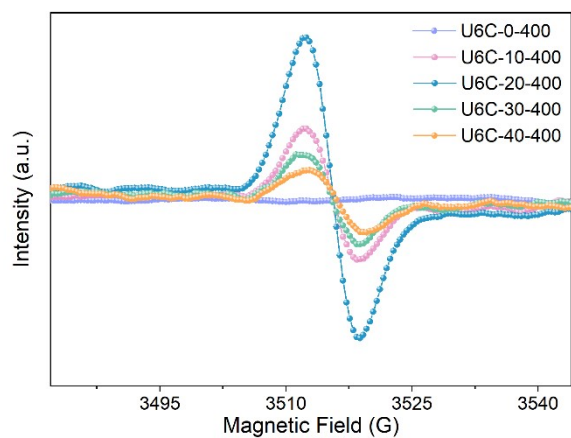


Figure S5. The EPR spectrum of U6C-0, U6C-10, U6C-20, U6C-30, and U6C-40 products are prepared by annealing at 400 °C.

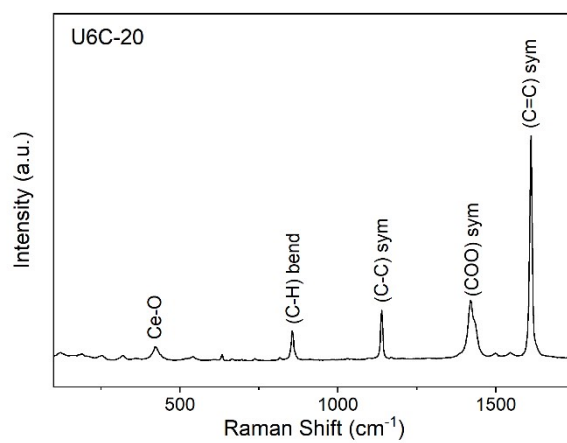


Figure S6. Raman spectra of U6C-20.

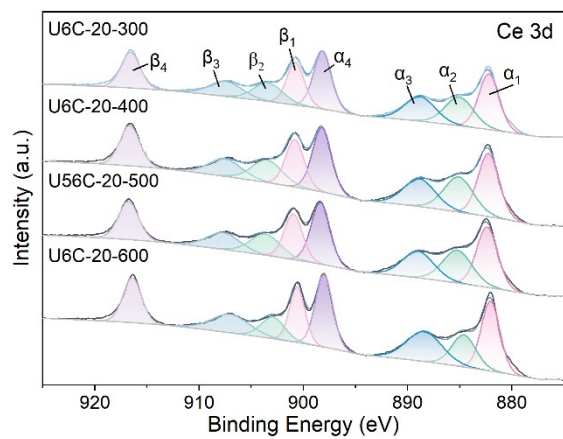


Figure S7. XPS Ce 3d high-resolution spectra of U6C-20-300, U6C-20-400, U6C-20-500, and U6C-20-600.

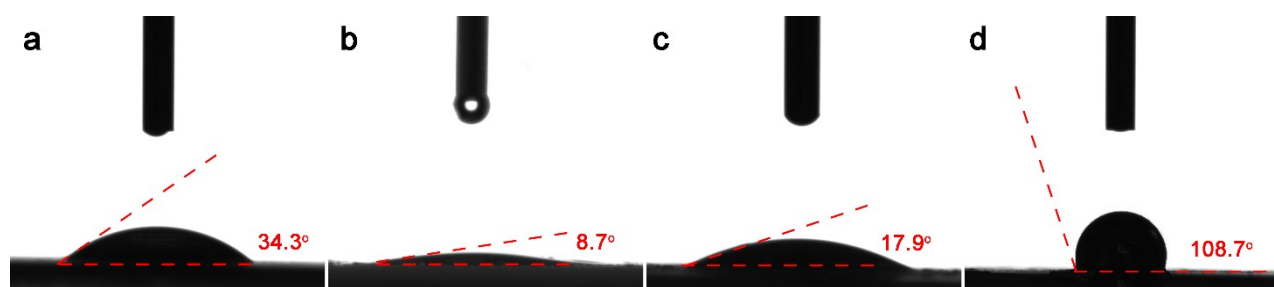


Figure S8. The contact angle of (a) U6C-20-300, (b) U6C-20-400, (c) U6C-20-500 and (d) U6C-20-600.

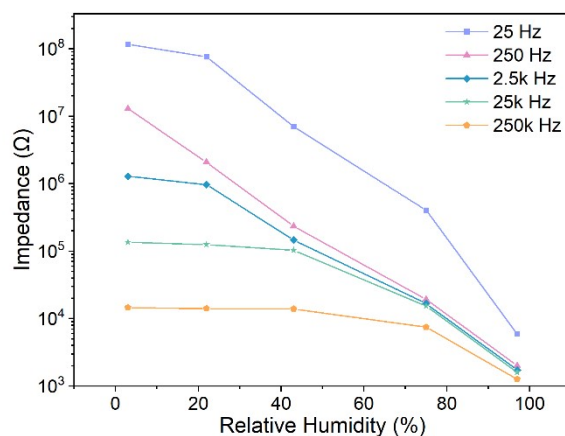


Figure S9. Frequency characteristic curve of U6C-20-400.

Test the sensor's performance at different alternating current (AC) frequencies (25 Hz, 250 Hz, 2.5k Hz, 25k Hz, and 250k Hz) to determine the optimum operating frequency of the sensor. It is clear from Figure S9 that the lower the operating frequency of the U6C-20-400 sensor, the higher its response in the same humidity environment. However, when the sensor's operating frequency is 25 Hz, the sensor's response is the highest, but the sensor's impedance value exhibits unstable fluctuations, making it difficult to measure accurately. The comprehensive comparison of humidity performance in the 3-97 % RH range determined that the best operating frequency was 250 Hz.

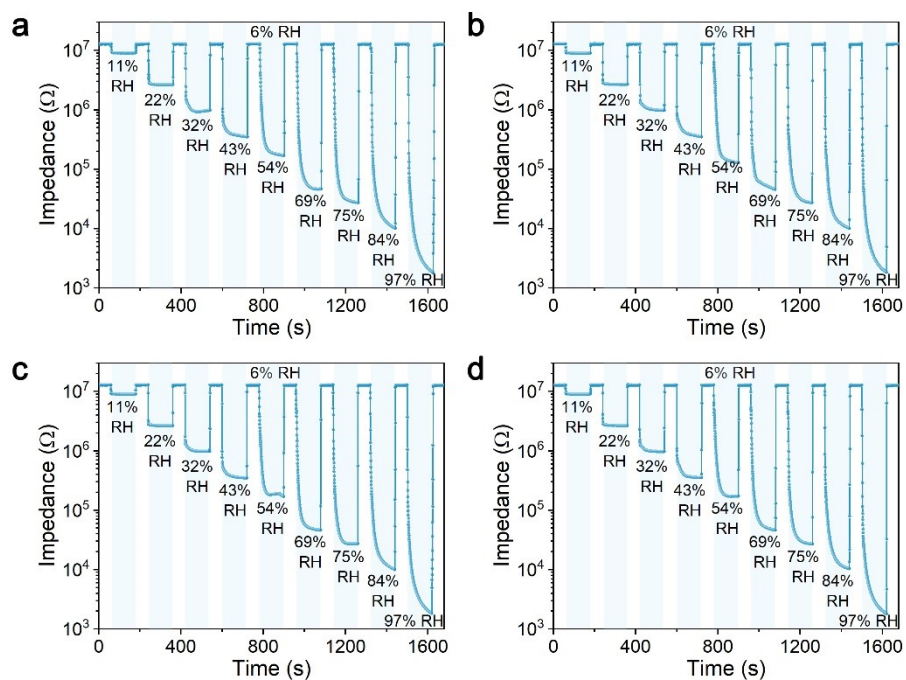


Figure S10. Continuous response recovery curves of U6C-20-400 in the humidity range of 6% RH to 97% RH at (a) week 1, (b) week 2, (c) week 3, and (d) week 4.

Figure S10 presents the test curves of the U6C-20-400 sensor for four consecutive weeks of humidity tests at different RH levels. It can be seen that the response values of the sensor from 6% RH to 11% RH, 22% RH, 32% RH, 43% RH, 54% RH, 63% RH, 75% RH, 84% RH, and 97% RH for four tests are (2,2,2,2), (5,5,5,5), (13,13,13,13), (37,36,37,35), (76,75,100,73), (276,278,284,280), (468,467,471,477), (1275,1278,1273,1244) and (6209,6041,6021,6123).

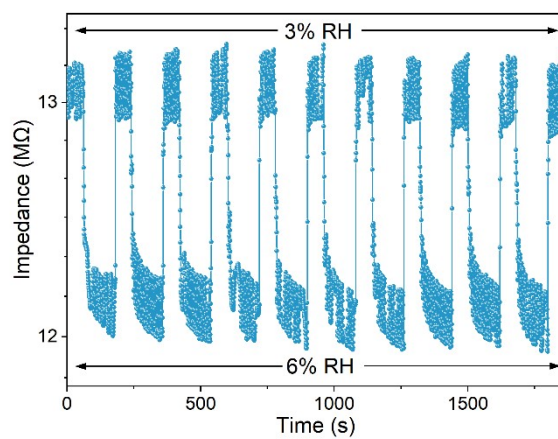


Figure S11. Multiple response recovery curves of U6C-20-400 sensors in the 3-6 % RH range.

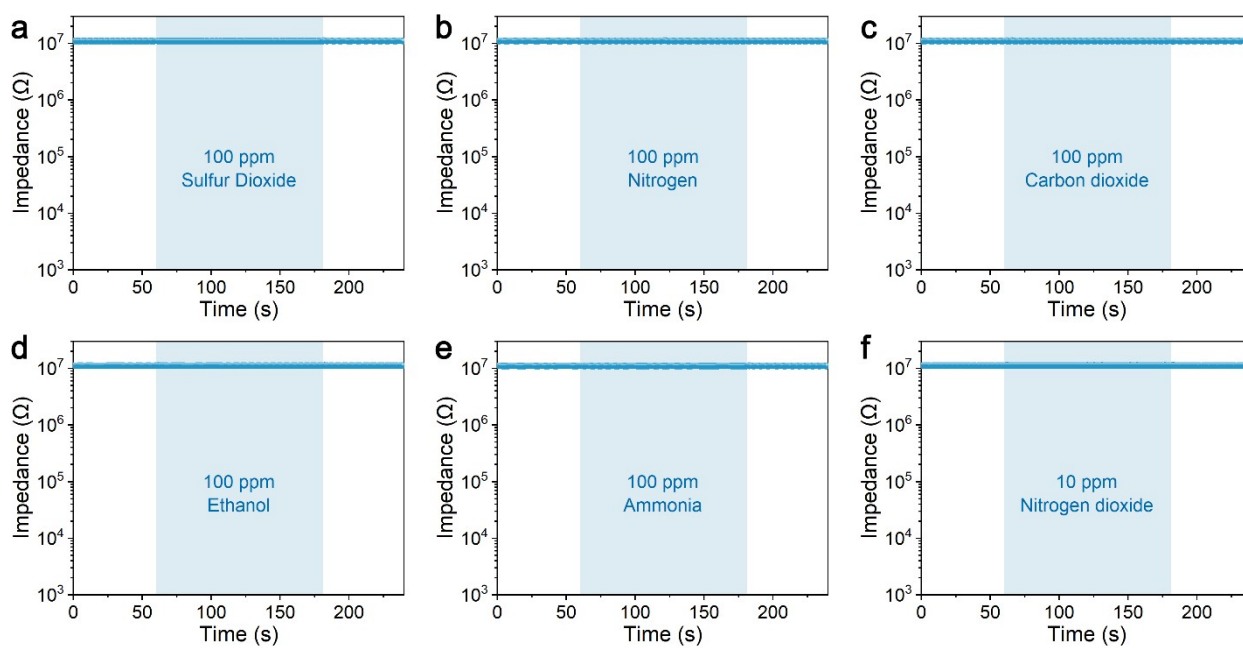


Figure S12. At 25 °C and 250 Hz, the selectivity testing of the U6C-20-400 sensor for 100 ppm (a) sulfur dioxide, (b) nitrogen, (c) carbon dioxide, (d) ethanol, (e) ammonia, and 10 ppm (f) nitrogen dioxide.

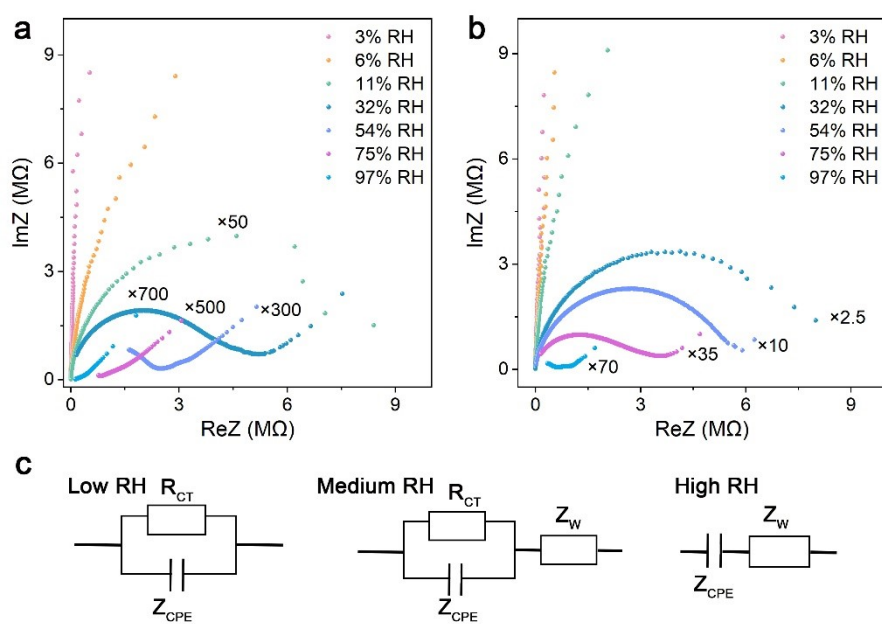


Figure S13. (a) Complex impedance spectra of U6C-20-400 at different humidity conditions; (b) Complex impedance spectra of U6C-20-600 at different humidity conditions; (c) Equivalent circuit diagrams for low humidity, medium humidity, and high humidity conditions.

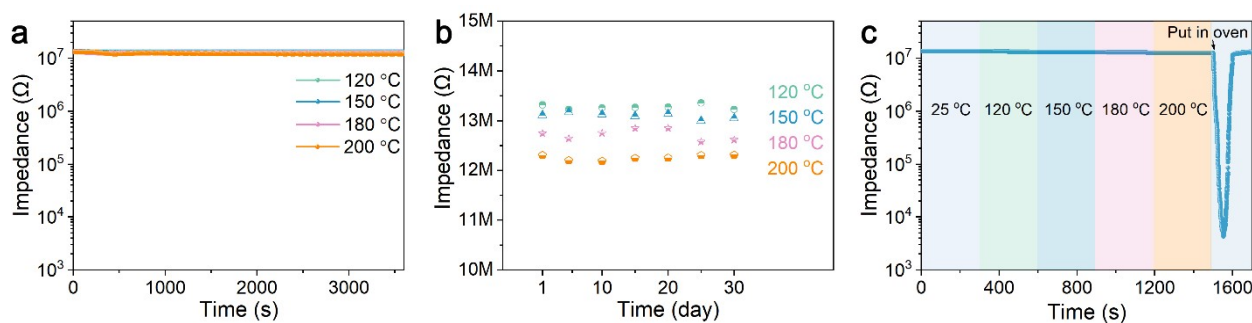


Figure S14. (a) Stability test of the U6C-20-400 humidity sensor at 120 °C, 150 °C, 180 °C, and 200 °C for 60 minutes; (b) Long-term stability test of the U6C-20-400 humidity sensor at various temperatures; (c) Impedance change of the U6C-20-400 humidity sensor at various baking temperatures (without food, with a baking time of 5 minutes at each temperature) and at 200 °C for bread slices.

Figure S14 illustrates the long-term high temperature stability of U6C-20-400 at different temperatures. Continuous 60 min testing of the U6C-20-400 sensor at 120 °C, 150 °C, 180 °C, and 200 °C (Figure 14a) reveals minimal variation in impedance under high temperature conditions. Further validation via a 30-day test (conducted every 5 days, Figure 14b) demonstrates exceptionally low relative standard deviations (RSDs) of impedance: 0.33%, 0.41%, 0.79%, and 0.37% at the respective temperatures. Additionally, monitoring curves from the bread-baking application at different temperatures (Figure S14c) show negligible temperature interference and superior detection capability, corroborating the sensor's thermal stability.

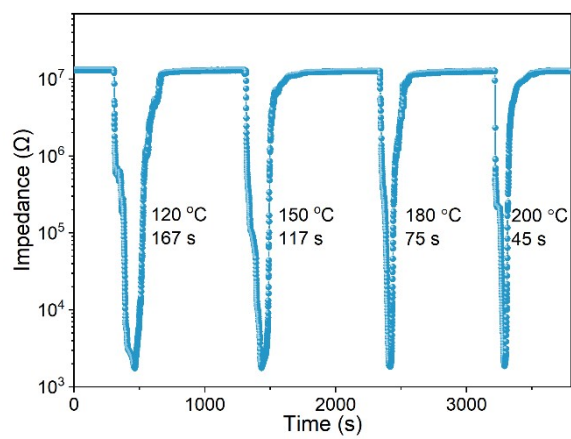


Figure S15. A repeatability test of U6C-20-400 was performed to monitor humidity changes caused by baking bread slices at different temperatures.

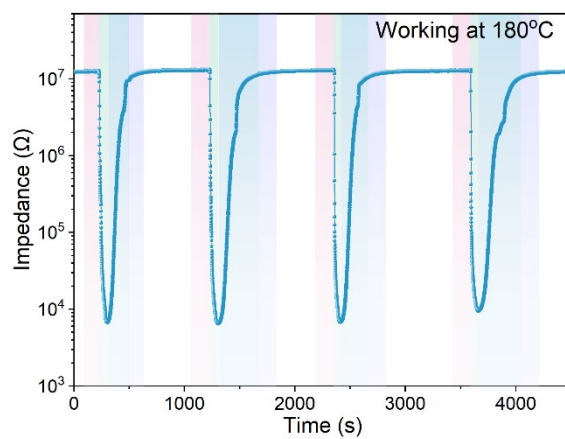


Figure S16. A repeatability test of U6C-20-400 was performed to monitor humidity changes caused by baking bread slices at the same temperature (180 °C).

Table S1. Analysis of XPS surface species with different acetic acid additions.

Samples	Ce ⁴⁺ (%)	Ce ³⁺ (%)	O _v (%)	O _{cco} (%)
U6C-0	63.06	36.94	7.50	78.71
U6C-10	58.98	41.02	12.98	66.94
U6C-20	53.86	46.14	15.19	64.14
U6C-30	61.79	38.21	10.62	69.76
U6C-40	62.05	37.95	8.70	72.26

Table S2. Oxygen vacancy content of U6C-20-300, U6C-20-400, U6C-20-500, and U6C-20-600 ($I_D/I_{F_{2g}}$).

Samples	$I_D/I_{F_{2g}}$ (%)
U6C-20-300	2.9
U6C-20-400	15.8
U6C-20-500	9.9
U6C-20-600	0.2

Table S3. The element composition and state of U6C-20-300, U6C-20-400, U6C-20-500, and U6C-20-600 as determined by XPS.

Materials	Ce ³⁺ /Ce ⁴⁺ (%)	O _{latt} (%)	O _V (%)	O _{OH} (%)
U6C-20-300	27.92	71.69	16.39	11.92
U6C-20-400	30.19	63.82	22.09	14.09
U6C-20-500	29.46	67.96	19.75	12.29
U6C-20-600	21.37	77.38	12.08	10.53

Table S4. Performance comparison of octahedral CeO₂ humidity sensor with other humidity sensors.

Material	Measurement range (% RH)	tres /trec (s)	Sensitivity	Ref.
CeO ₂ /IL	11-97	4/<1	105	[1]
CeO ₂ nanoparticles	11-98	10/3	8837	[2]
Ag/TiO ₂	11-95	31/15	39707	[3]
CeO ₂ nanoparticles	11-97	2/9	103	[4]
Fe/SnO ₂	11-95	10/8	145290	[5]
CeO ₂ nanosheets	11-97	11/183	31000	[6]
CeO ₂ nanoparticles	11-97	3/16	103	[7]
Ag/SnO ₂	11-95	5/8	24292	[8]
Au/ZnO nanosheets	11-95	16/28	100000	[9]
CeO ₂ nanoparticles	11-98	4.3/2.7	104.5	[10]
h-WO ₃	11-95	1.5/15.1	2919	[11]
Nest-like CeO ₂	11-97	0.5 /4.3	6565	[12]
KCl/Sm ₂ O ₃ nanoflowers	11-95	0.1/21	127121	[13]
Ho ₂ O ₃ nanosheets	11-95	0.3/6	1143	[14]
Dy ₂ O ₃ 3D tube-globular	11-95	0.35/17	1300	[15]
Ho ₂ O ₃ /GO	11-97	0.2/1	2136	[16]
Er ₂ O ₃ nanospheres	11-93	1/5.1	403	[17]
Octahedral CeO ₂	3-97	0.5/1.2	6058	This work

References

1. Xie W. Y.; Duan X. C.; Deng J. W.; Nie J. X.; Wang T. H. CeO₂/ionic liquid hybrid materials with enhanced humidity performance. *Sens. Actuators B* **2017**, 252, 870-876.
2. Xie W. Y.; Liu B.; Xiao S. H.; Li H.; Wang Y. R.; Cai D. P.; Wang D. D.; Wang L. L.; Liu Y.; Li Q. H.; Wang T. H. High performance humidity sensors based on CeO₂ nanoparticles. *Sens. Actuators B* **2015**, 215, 125-132.
3. Yang C.; Zhang H. Y.; Gu W. Y.; Chen C. Preparation and mechanism investigation of highly sensitive humidity sensor based on Ag/TiO₂. *Curr. Appl. Phys.* **2022**, 43, 57-65.
4. Khadse V. R.; Thakur S.; Patil K. R.; Patil P. Humidity-sensing studies of cerium oxide nanoparticles synthesized by non-isothermal precipitation. *Sens. Actuators B* **2014**, 203, 229-238.
5. Zhang H. Y.; Zhang H. Y.; Man J. P.; Chen C. Preparation of high performance Fe-doped SnO₂ humidity sensor and its application in respiration detection. *Sens. Actuators A* **2023**, 362, 114644.
6. Zhang P.; Zhang L. X.; Xu H.; Xing Y.; Chen J. J.; Bie L. J. Ultrathin CeO₂ nanosheets as bifunctional sensing materials for humidity and formaldehyde detection. *Rare Met.* **2020**, 7, 01619.
7. Thakur S.; Patil P. Rapid synthesis of cerium oxide nanoparticles with superior humidity-sensing performance. *Sens. Actuators B* **2014**, 194, 260-268.
8. Zhang H. Y.; Zhang H. Y.; Chen C.; Zhang L.; Ma X. J.; Li X. D.; Wang J. Preparation of silver nanoparticles modified SnO₂ humidity sensor for tobacco storage environment detection. *Sens. Actuators B* **2024**, 409, 135612.
9. Yu S. G.; Zhang H. Y.; Chen C.; Lin C. C. Investigation of humidity sensor based on Au modified ZnO nanosheets via hydrothermal method and first principle. *Sens. Actuators B* **2019**, 287, 526-534.
10. Poonia E.; Mishra P. K.; Kiran V.; Sangwan J.; Kumar R.; Rai P. K.; Malik R.; Tomer V. K.; Ahuja R.; Mishra Y. K. Aero-gel based CeO₂ nanoparticles: synthesis, structural properties and detailed humidity sensing response. *J. Mater. Chem. C* **2019**, 7, 5477.

11. Guo P. W.; Tian B.; Liang J.; Yang X. P.; Tang G. L.; Li Q. C.; Liu Q.; Zheng K.; Chen X.; Wu W. An All-Printed, Fast-Response Flexible Humidity Sensor Based on Hexagonal-WO₃ Nanowires for Multifunctional Applications. *Adv. Mater.* **2023**, 2304420.
12. Li H. X.; Liu Y.; Zhang X. F.; Guo C. Y.; Zhang H. M.; Zhao X. L.; Huo L. H.; Dong X.; Huang C. B.; Cheng X. L.; Xu Y. M. Preparation of nest-like CeO₂ humidity sensing material and its application in eye strain monitoring. *Sens. Actuators B* **2024**, 415, 135985.
13. Na B. Y.; Guo C. Y.; Wang T. T.; Zhang X. F.; Huo L. H.; Li L.; Liu Y.; Cheng X. L.; Xu Y. M. Multifunctional and highly sensitive humidity sensor based on KCl/Sm₂O₃ nanoflowers with ultrafast response. *Sens. Actuators B* **2023**, 385, 133701.
14. Guo C. Y.; Dong X.; Zhang X. F.; Cheng X. L.; Li Q.; Sun Y. J.; Liu W.; Huo L. H.; Xu Y. M. Controllable construction of Ho₂O₃ nanomaterials with different dimensions (1D, 2D, and 3D) for real-time monitoring human breathing and body surface humidity detection. *J. Mater. Chem. A* **2021**, 9, 11632.
15. Hu Q. C.; Cheng X. L.; Zhang X. F.; Xu Y. M.; Gao S.; Zhao H.; Major Z.; Huo L. H. One-step solvothermal synthesis of 3D tube-globular Dy₂O₃ nanostructure for ultra-fast response to humidity. *Sens. Actuators B* **2020**, 305, 127434.
16. Guo C. Y.; Xin Y. Y.; Liu Y.; Na B. Y.; Meng W. Q.; Zhang X. F.; Cheng X. L.; Huo L. H.; Wang T. T.; Xu Y. M. Noncontact sensing for water area scanning identification based on Ho₂O₃/GO humidity sensor. *Sens. Actuators B* **2023**, 385, 133683.
17. Jiang Y. F.; Guo C. Y.; Zhang X. F.; Cheng X. L.; Huo L. H.; Wang T. T.; Xu Y. M. Er₂O₃ nanospheres with fast response to humidity for non-contact sensing. *Rare Met.* **2023**, 42, 56-63.